Measurement of particle yields induced by 200-MeV protons on multiple targets

Bachelor's Thesis

Author: Antonio Lopez

6 months 15 hp

Supervisors: Joochun Park and Joakim Cederkäll

Lund University

VT 2018

Abbreviations

APD	Avalanche PhotoDiode
CALIFA	CALorimeter For In Flight detection of γ rays and high energy charged pArticles.
CCB	Centrum Cyklotronowe Bronowice
DA	Technical University Darmstadt
DAQ	Data AcQuisition
DSSSD	Double-Sided Silicon Strip Detector
FAIR	Facility for Antiproton and Ion Research
GLAD	GSI Large Acceptance Dipole
GSI	Gesellschaft für Schwerionenforschung
IS	Intrinsic Semiconductor
LAND	Large-Area Neutron Detector
LU	Lund University
NUSTAR	Nuclear Structure, Astrophysics and Reactions
QFS	Quasi-Free Scattering
R^3B	Reactions with Relativistic Radioactive Beams
RPID	Reconstructive Particle IDentification

Contents

Abstract

One way to probe the structure of atomic nuclei far from stability is via quasi-free scattering (QFS) reactions. We conducted a (p,2p) QFS experiment on H_2O, ^{112}Sn, ^{124}Sn and ^{208}Pb targets in order to test the performance of CsI(Tl) detectors that are to be used in the upcoming R^{3}B experiments at FAIR. With the help of particle tracking and reconstructive particle identification (RPID) cuts based on CsI(Tl) and Si detector data, we identified different light particle yields from the targets and (p,2p) events. An indication of a (p,2p) reaction to the ground state of ^{111}In was observed from the ^{112}Sn target. Furthermore, a 6.3-MeV γ ray was seen in coincidence with (p,2p) events in the H_2O target. This corresponds to the $3/2^- \to 1/2^-$ transition energy in ^{15}N. The experiment was therefore successful in detecting (p,2p) reactions using the new detector systems and at the same time gave directions for future studies.

1

1 Introduction

1.1 Physics background and motivation

The structure of atomic nuclei can be studied with nuclear spectroscopy using nuclear scattering experiments. In a scattering experiment nuclear reactions can take place between the incident beam and the target particles. The target can be anything from a single nucleon to heavy elements, such as ^{208}Pb. Nuclear reactions can be defined as elastic, in which the kinetic energy is conserved, or inelastic, in which kinetic energy is used to create and excite the residual nuclei.
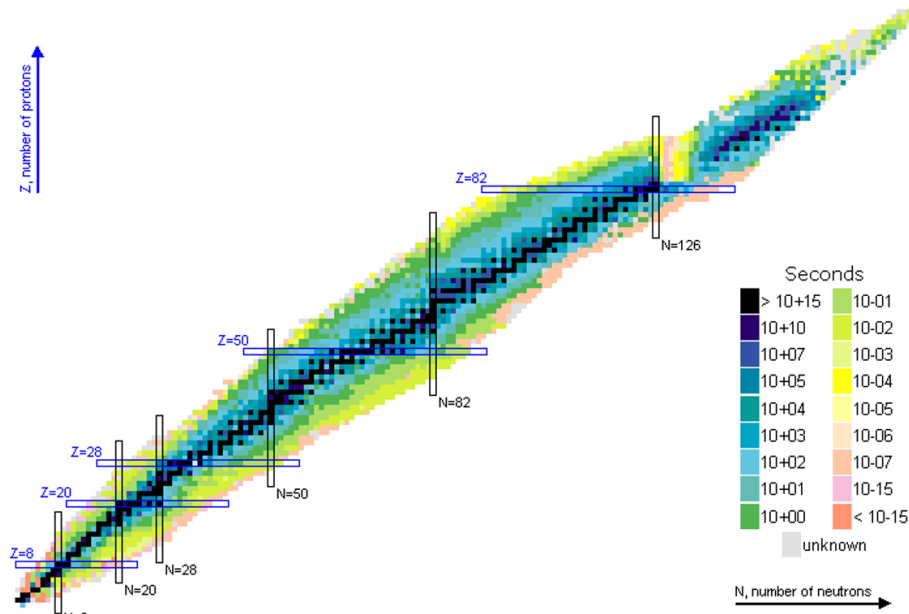

Figure 1: The chart of nuclides with horizontal and vertical lines indicating nuclear shell closures for neutrons and protons. This study focused on investigating proton elastic and quasi-free scattering on ^{16}O , but reactions with ^{112}Sn, ^{124}Sn and ^{208}Pb were also studied [1].

As an analogy to classical physics, one can imagine two spheres of known dimensions colliding, resulting in an energy loss in the form of heat production. In nuclear physics the inelastic case is often more interesting as the excited nuclei can emit γ rays and/or individual-, or clusters-, of nucleons. This radiation gives information about the reaction products and their internal structure. Depending on the masses and energies of the involved parties, a new distribution of momenta will result and give new energies and trajectories for the outgoing particles. Consequently, by carrying out experiments of this kind and analysing the energy spectra of the scattered particles and emitted photons, we can gain a better understanding of nuclear shell structure, valence-nucleon wavefunctions, single-particle properties and nucleon-nucleon correlations, etc. [2].

Currently an active research topic in experimental nuclear physics is to study the structure of nuclei far from stability using scattering reactions. Since it is impractical to use short-lived nuclei as targets, it leads to the need to use beams consisting of radioactive isotopes. This is particularly true in cases of (p,2p) reactions for systems far beyond the line of stability, where a proton is knocked out from the beam particle. Experiments of this kind will be performed in the upcoming Facility for Antiproton and Ion Research (FAIR) via the Reactions with Relativistic Radioactive Beams (R^3B) experiment. Figure 1 shows the chart of nuclides and the half-lives of the unstable isotopes. In this context, particularly interesting is the behaviour of semi-magic and magic nuclei on the neutron-rich side which, for instance, is of importance to better understand the r-process in nuclear astrophysics [3].

1.2 The Facility for Antiproton and Ion Research - FAIR

FAIR is an international accelerator facility under construction in Darmstadt, Germany. It is placed at the site of the Gesellschaft für Schwerionenforschung (GSI) and can be seen as an expansion of this facility (see Figure 2). By performing experiments with large-scale accelerators and ion-colliders, six new chemical elements have been discovered at GSI and also a new type of tumor therapy using ion beams [5] has been developed in the past. Currently the work at GSI focuses on basic research in nuclear- and atomic physics, while applied scientific research is also carried out in areas such as material-, plasma-, bio- and medical physics [5].

FAIR will provide high energy heavy ion beams up to 45 GeV/u [6] and anti-protons in the ~GeV range, and will consist of four main research pillars:

- APPA (Atomic, Plasma Physics and Applications)
- CBM (Compressed Baryonic Matter)
- NUSTAR (Nuclear Structure, Astrophysics and Reactions)
- PANDA (Antiproton Annihilation at Darmstadt)

Some experiments associated with APPA are collisions of high Z ions moving at relativistic speeds. At these velocities one can generate high-intensity photon fields from the collision of said ions, in order to better understand Quantum ElectroDynamics (QED) [7]. CBM, on the other hand, deals with high density states of nucleons and other properties of Quantum ChromoDynamics (QCD), such as phase transitions and chirality [8]. Other topics of research at FAIR involve colliding protons and antiprotons (PANDA), in which one will be able to create particles such as Charmonium [9]. By performing spectroscopic studies of their decays one will gain new understanding of the behaviour of the strong force and quark confinement.

This study involves the Reactions with Relativistic Radioactive Beams (R^3B) experiment
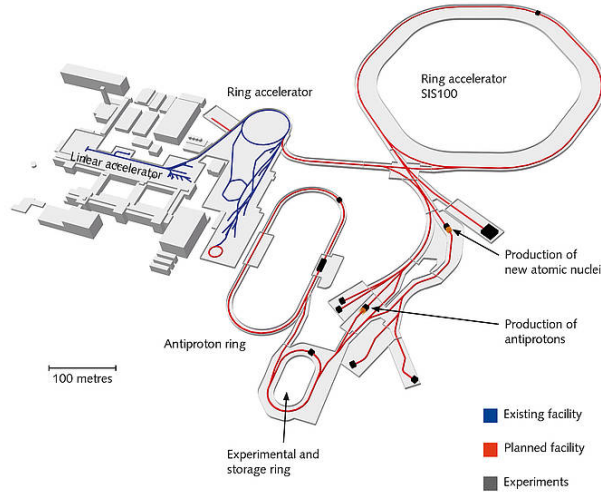
Figure 2: Overview showing the existing facility at GSI (in blue) and the upcoming FAIR (in red) [4].

which is part of the NUSTAR pillar. One aim of R^3B is to make use of reactions in inverse kinematics by accelerating heavy ions onto light targets and measure the de-excitation of residual nuclei and their recoil momenta [10]. Due to the high energies, inverse kinematics provides easier measurements of the outgoing particles, energies and momenta compared to direct kinematics.

1.3 The R^3B experiment

NUSTAR is a collaboration of the nuclear structure and astrophysics communities, aiming to conduct experiments in their respective fields at the FAIR facility. Some of the goals of the R^3B experiment are to address exotic structures in nuclei, weakening of the shell structures, evolution of single-particle structure and nuclear deformation [11].

R^3B features a versatile multi-purpose experimental setup that will allow measurements of large energy-induced reactions with high resolution and efficiency. The R^3B detection system is a new design based on experience from the ALADIN-LAND experiment [12]. A schematic of the R^3B experiment is shown in Figure 3. It consists of the following main components:

- Si tracker - Consists of up to 30 semiconductor detectors in three layers with a total active area of $\sim$0.56 m^2. It has approximately 100000 front-end channels, and an angular coverage of $6°$ - $103°$, allowing it to track recoiling particles and find primary vertices [13].

- CALIFA (CALorimeter for In Flight detection of γ rays and high energy charged pArticles) - Scintillation detector system used in the experiment, described further

4

in section 3.4.

- GLAD (GSI Large Acceptance Dipole) - Capable of magnetic fields up to 6 T and has an operational temperature and current of 4.6 K and 3.6 kA, respectively. It weighs $22 \cdot 10^3$ kg and has the dimensions 4.8 x 2.8 x 39 m^3 (width · height· length) [14].

- Scintillation fibre detectors for heavy outgoing fragments.

- NeuLAND - Plastic scintillator consisting of 3000 individual submodules of 5 x 5 x 250 cm^3 (width · height· length). The active area and depth are 250 x 250 cm^2 and 3 m, respectively. Designed in order to achieve 95% one-neutron detection efficiency [15].
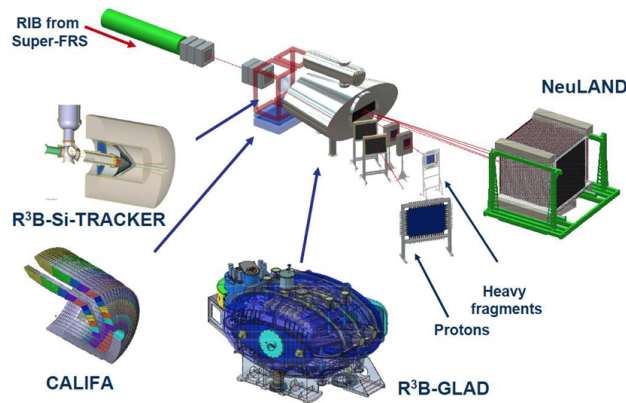

Figure 3: The R^{3}B experiment diagram. The combination of different detectors aims to detect as much of the outgoing radiation as possible for complete kinematic reconstruction. The five main components are: the silicon tracker for tracking outgoing particles and determining the position of the reaction vertex, CALIFA for detecting charged particles and γ rays, the magnet GLAD for separating charged fragments not caught by CALIFA based on their charge-to-mass ratio, the neutron detector NeuLAND (Large-Area Neutron Detector) and the tracking detectors for heavy ions and protons behind the GLAD magnet [12].

1.4   Aim of this study

The experiment described in this study was performed in order to test detector segments for CALIFA that have been developed for the R^{3}B experiment. The isotopes used as targets were ^{1}H, ^{16}O, ^{112}Sn, ^{124}Sn and ^{208}Pb. ^{16}O and ^{208}Pb are both considered to be part of the magic number group, as they both contain filled proton and neutron shells with $Z = N = 8$, $Z = 82$ and $N = 126$, respectively. This means that the nucleus has a higher-than-average binding energy per nucleon due to the major shells being filled. The Sn isotopes, on the other hand, belong to what is known as a semi-magic chain, as they only completely fill the proton shells with $Z = 50$, which is horizontally lined out in Figure 1.

The main aim of the study is to investigate particle and γ ray emission from (p,2p) and other reactions to extract quasi-free scattering amplitudes, to be compared. Particularly interesting is to measure differences in cross section for various reaction channels and targets, as this could give a deeper understanding of how the number of nucleons that occupy different orbits affect the nuclear structure.

2 Theoretical Introduction

2.1 Nuclear Shell Model

Nuclei can be modeled in a shell-like structure where the nucleons move in spatial orbits similar to that of the electrons in the atom. Furthermore, suppose that two nucleons deep inside the nucleus interact with each other, their kinetic energies would not be high enough to scatter either one of them up to or above the Fermi surface. Therefore, it would appear that they are moving independently.

From early observations, one noted that the nuclear potential could not be properly described by a harmonic oscillator, since such a model could not reproduce experimental nucleon separation energies or magic numbers. An obvious unphysical property of the harmonic oscillator is its infinite well since experimentally it is known that nucleons can be removed from the nucleus. Furthermore, the harmonic oscillator has the property that the levels with different orbital angular momentum quantum numbers, l, and the same principal quantum number, n, have the same energy, i.e. are degenerate. For this reason one often models the nucleus using a Woods-Saxon potential,

$$V(r) = \frac{-V_0}{1 + e^{(r-R)/a}},$$

(1)

where V_0 is the average nuclear potential, R is the radius and a is the skin thickness [16], since this lifts the l-degeneracy.

However, the shell ordering and the magic numbers are not properly reproduced using this potential alone either, which led to the introduction of a term that depends on the orientation of the spin with respect to the orbital angular momentum, so called ls-coupling. The inclusion of this spin-orbit term made it possible to properly separate the subshells into different j-levels with the capacity to hold $(2j + 1)$ nucleons [17].

In the extreme single particle model one assumes that nuclear properties largely depend on the unpaired nucleon in an odd-mass nucleus. If one defines the total angular momentum, j, as the sum of the orbital angular momentum and spin of the nucleon, $j = l + s$, then the spin and parity of the nucleus will be given by the unpaired nucleon with a spin
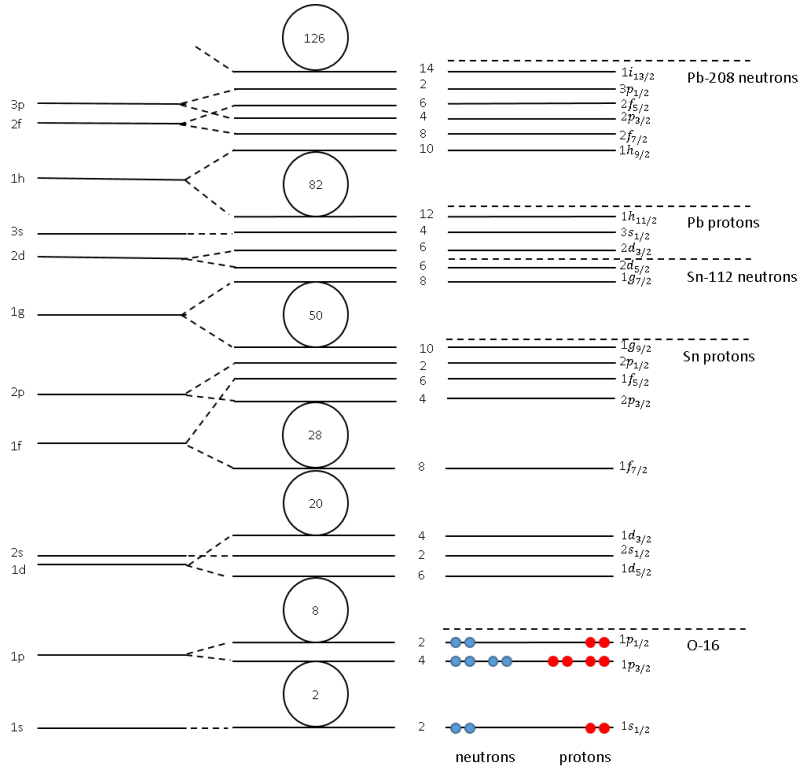
Figure 4: Nuclear shell structure [16]. The left side shows the energy levels calculated using the Woods-Saxon potential. The energy levels can be further separated taking spin-orbit interactions into consideration, as shown on the hand right side. The resulting energy gaps reproduce the experimental magic numbers.

j and parity $(-1)^l$. While the theory is rather simplified it is fairly successful in predicting nuclear properties, such as the ground state spin of odd-A nuclei [16].

The targets ^{16}O, ^{112}Sn and ^{208}Pb used in the experiment are indicated in Figure 4. Of these, ^{16}O and ^{208}Pb have magic numbers for neutrons and protons, while ^{112}Sn only has filled major proton shell. Consequently, these atomic nuclei are particularly well bound. By doing knock-out reactions on these isotopes we can investigate the states that are below the Fermi surface. In ^{16}O this would correspond to the protons in the p and s shells, in Sn the protons in or below $1g_{9/2}$ shell and correspondingly for ^{208}Pb, the $1h_{11/2}$. This is particularly interesting for experiments on isotopes far beyond the line of stability, in order to see if the states below the Fermi surface have the same ordering as for isotopes at the line of stability. A way to investigate this experimentalty is discussed in section 2.2.
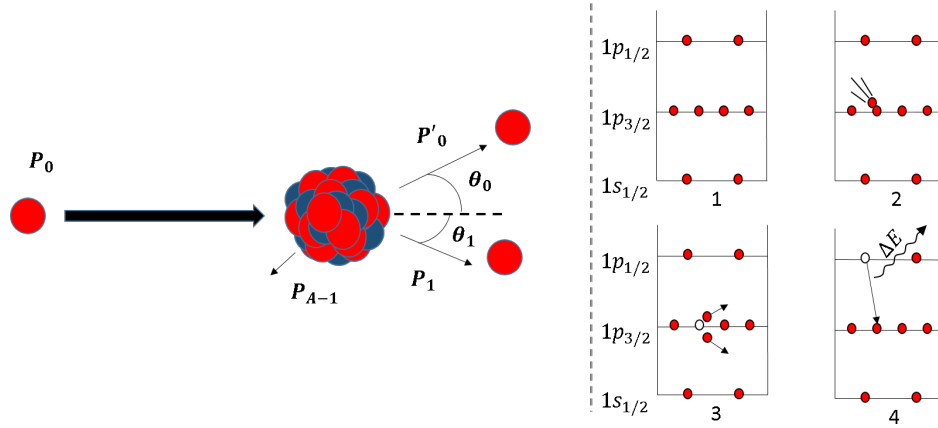
7

2.2 Quasi-Free Scattering - QFS

Figure 5: The left panel illustrates an incident proton with momentum $\mathbf{P}_0$ sent towards a target nucleus, knocking out a proton. The two protons obtain the momenta $\mathbf{P'}_0$ and $\mathbf{P}_1$. Furthermore, the nucleus is left with a recoil momentum corresponding to $\mathbf{P}_{A-1}$. In the right panel, a simplified shell model is used to illustrate in four steps the knock-out reaction for ^{16}O(p,2p)^{15}N. The undisturbed system of the proton shells (1). An incident proton collides with a proton in the $1p_{3/2}$ shell (2). The $1p_{3/2}$ proton is knocked out and the incident proton changes trajectory (3). A proton from the $1p_{1/2}$ shell occupies the hole, resulting in the emission of a γ-ray (4).

By accelerating a proton beam to intermediate energies of 200-1000 MeV one can induce (p,pN) knock-out reactions, where N can be either a neutron, a proton or a cluster of nucleons. Figure 5 illustrates a specific case of a (p,2p) reaction which is a possible outcome of a knock-out reaction. When a nucleon is emitted it leaves behind a hole in the shell. If another nucleon is in a less bound state, it will promptly occupy the vacancy and a photon will be emitted with an energy equal to the difference between the initial and final states.

In addition to (p,2p) knock-out, we also expect to observe other particles emitted as a result of the reaction, such as neutrons (if neutron detectors are available) and deuterons, tritons, ^{3}He and alpha-particles.

In a (p,2p) reaction the minimum energy required to knock out a proton is called the proton separation energy, S_p. All events of such reactions are therefore inelastic. Sometimes, the residual nucleus is left in an excited state resulting in a subsequent emission of γ-rays. Therefore the resulting kinematics after a (p,2p) event gives a relation between the initial and final state energies. In the following equations the incident and two emitted protons are denoted as $0, 0'$ and 1, respectively. Furthermore, the index A and $(A-1)$ refers to the nucleus, initial and final states. The proton separation energy can be defined in relation to the kinetic energies of the involved parties as [18],

$$S_p = T_0 - (T'_0 + T_1 + T_{A-1}) \tag{2}$$

where T is the kinetic energy of a particle assuming that the initial state of the nucleus is at rest. Invoking the conservation of energy and momentum, we have,

$$E_0 + m_A c^2 = E'_0 + E_1 + E_{A-1} \tag{3}$$

$$\mathbf{P_0} = \mathbf{P'_0} + \mathbf{P_1} + \mathbf{P_{A-1}} \tag{4}$$

where the total energy of a given particle is defined by,

$$E = mc^2 + E_{exc} + T \tag{5}$$

where E_{exc} is the excitation energy of the final nucleus [18]. The charged particles and their momenta are then measured by dedicated detectors situated around the target. In our case, segments of the CALIFA detector were used for this purpose. In these intermediate energy ranges relativistic kinematic is used.

3 Experimental Background

Experiments of the kind discussed above rely on the capacity to identify charged particles and photons and measure their energies. The calorimeter, CALIFA, is a scintillation detector and has been specifically designed for the upcoming FAIR facility in order to have higher efficiencies and energy resolutions for γ-radiation and light particles than its predecessor, the Crystal ball spectrometer. To detect and track the particles we used a combination of CsI(Tl) scintillation and Double Sided Silicon Strip (DSSSD) detectors in the experiment. Consequently, it is important to understand the underlying principles of how charged particles and photons interact with the detector material.

3.1 Charged particle and γ-ray interaction with matter

Charged particles that traverse a detector material lose energy due to collisions, as described by Bethe-Bloch formula eq. 6,

$$-\frac{dE}{dx} = 2\pi N_a r_e^2 m_e c^2 \rho \frac{Z}{A} \cdot \frac{z^2}{\beta^2} \left[ln \left(\frac{2m_e \gamma^2 \mu^2 W_{max}}{I^2} \right) - \beta^2 - \sigma - 2\frac{C}{Z} \right] \tag{6}$$

9

with r_e being the radius of the electron; m_e the rest mass of the electron; N_a Avogadro's number; W_{max} the maximum energy transfer per collision; z the incident particle charge; ρ the density of material; β: $\frac{v}{c}$ of incident particle; γ: $\frac{1}{\sqrt{1-\beta}}$; Z: atomic number of absorbing material; A: atomic mass of absorbing material; C: shell correction; σ: density effect correction; I: average excitation potential . There are additional formulas and tables to calculate certain terms such as C, I, W_{max}, etc [19].

As photons are electrically neutral, their energy loss cannot be described by the Bethe-Bloch formula. Instead, they undergo one of three processes: Compton scattering, pair production and the photoelectric effect.

Compton scattering involves the inelastic scattering of a photon and an electron. In the reaction, the electron receives part of the photons' energy and may be knocked out of its shell, leaving the photon with a lower energy, as given by eq. 7,

$$E' = \frac{E}{1 + \gamma(1 - \cos\theta)} \tag{7}$$

with $\gamma = \frac{E}{m_e c^2}$ and θ being the scattering angle of the photon [19]. The equation shows that the photons' final energy depends not only on its initial energy, but also on its scattering angle. Furthermore, the final energy of the electron will be given as the difference of the initial and final photon energies and can be written as eq. 8,

$$T = E - E' = E \frac{\gamma(1 - \cos\theta)}{1 + \gamma(1 - \cos\theta)} \tag{8}$$

To calculate the cross section for Compton scattering one can use the Klein-Nishina formula (eq. 9), where r_e is the electron radius [19],

$$\frac{d\sigma}{d\Omega} = \frac{r_e^2}{2} \frac{1}{[1 + \gamma(1 - \cos\theta)]^2} \left(1 + \cos^2\theta + \frac{\gamma^2(1 - \cos\theta)^2}{1 + \gamma(1 - \cos\theta)} \right). \tag{9}$$

If the photon has high enough energy ($\geq 2\ m_e c^2$) it can convert into an electron and a positron. This transformation is known as a pair production and occurs in the presence of a nucleus in order to ensure momentum conservation. Equation 10 describes pair production in the presence of an isotope X,

$$\gamma + X \rightarrow e^- + e^+ + X^* \tag{10}$$

where X and X^* describe the ground- and excited state of the nucleus [22]. In higher energy ranges (≥ 20 MeV) the pair production cross section is proportional to the square of the atomic number of the detector material and can be written as,
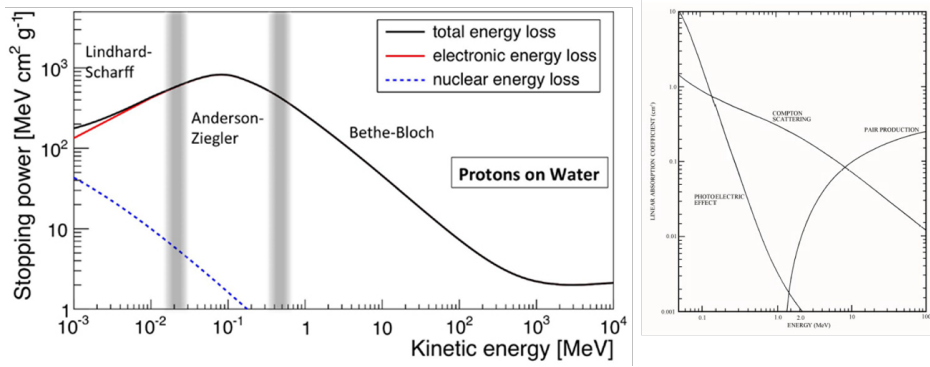
Figure 6: Left panel: proton stopping power in H_2O. Right panel: comparison of probabilities for γ-ray interaction with matter: Compton scattering, pair production and photoelectric effect [20, 21]

.

$$\sigma_{pair} = 4\alpha r_e^2 Z^2 \left(\frac{7}{9} ln \frac{183}{Z^{1/3}} - \frac{1}{54} \right) \tag{11}$$

where α is the fine structure of the electron [22].

In the photoelectric effect the entire energy of a photon is transferred to an electron, usually making it unbound and move freely in the material. However, the probability of the photoelectric effect in the higher energy ranges is quite low compared to Compton scattering and pair production, as shown in Figure 6. Consequently, the photon is typically required to Compton scatter or undergo pair production before the photoelectric effect becomes dominant, producing multiple interaction points where the fragmented energies have to be properly summed to recover the incoming photon energy.

3.2 Scintillator detectors

As charged particles pass through a scintillator, the electrons of the material become excited. When the electrons relax to the ground state, a number of photons is emitted that is proportional to the energy deposited by radiation in the material. The light output of a scintillator is registered by a photosensor. The resulting signal can be measured by an appropriate setup of electronics connected to the detector. In more detail, when a valence electron is excited to the conduction band in an inorganic scintillator crystal, it leaves behind a hole. This will result in an electron-hole pair known as an exciton which is partially bound. Eventually the pair recombines leading to the emission of photons as shown in Figure 7. By introducing impurities known as activators one can reduce the chance of self-absorption, as otherwise forbidden energy ranges become available in the gap. Self-absorption is an event where photons excite other electrons instead of being transmitted
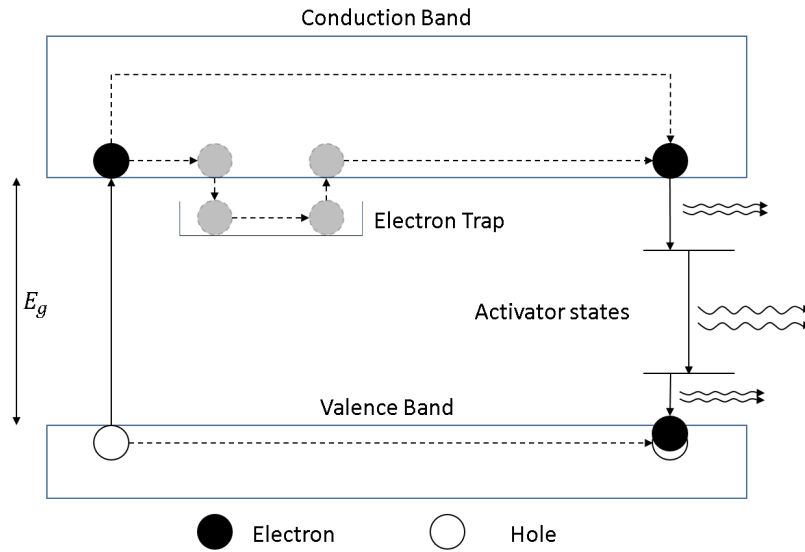
Figure 7: Excitation mechanism of an inorganic crystal scintillator [22]. Electrons in the conduction band may fall into electron traps, delaying photon emission. Eventually it returns to the conduction band and undergoes a series of de-excitations. As these photons each have less energy than the bandgap E_g, they are unable to excite other electrons in the material.

through the scintillating material. Furthermore, activators also lead to the formation of metastable states known as electron traps, which are important for formation of fast and slow components of the signal for some scintillators [22].

Mathematically, in the case of two components, the light emission can be described by eq. 12 [19]. If $L(t)$ defines the light emission as a function of time t, τ is the decay time constant, N corresponds to the amplitude, and subscripts f and s indicate fast/slow scintillation components, then,

$$L(t) = \frac{N_f}{\tau_f} \cdot e^{-\frac{t}{\tau_f}} + \frac{N_s}{\tau_s} \cdot e^{-\frac{t}{\tau_s}}. \tag{12}$$

An advantage of multi-component scintillators is the possibility to distinguish particles due to the different overall pulse shapes they give rise to. For instance, it is found that in CsI(Tl) scintillators the overall decay time is 0.425 μs for α particles and 0.519 μs for protons [19].
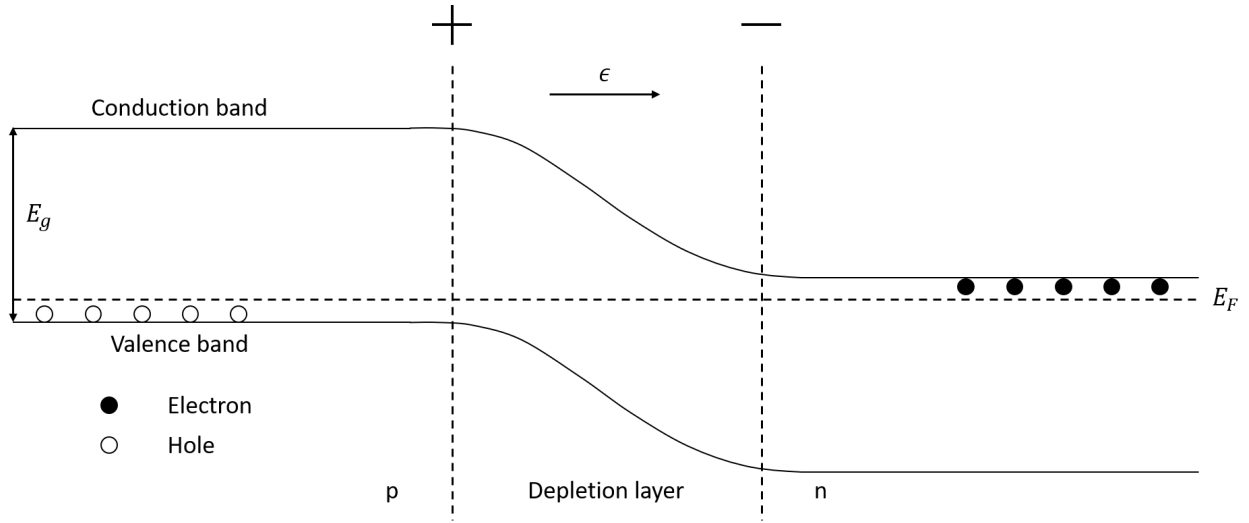
3.3 Semiconductor detectors

Figure 8: Semiconductor P-N junction [19]. When the P-N materials come into contact, electrons and holes diffuse and create a depletion region, consequently generating an internal electric field.

Intrinsic semiconductors (IS) are pure crystalline solids with four valence electrons, such as Si and Ge. The excitation mechanism resembles that of the inorganic crystal scintillator with the excitation of valence electrons to the conduction band and their subsequent relaxation. The occupation of energy states in the IS is defined by the Boltzmann distribution function which depends on the temperature, as given by eq. 13,

$$f(E,T) = \frac{1}{e^{(E-E_F)/k_B T} + 1},$$
(13)

where E_F is the Fermi energy, E is the energy of a specific state and T is the absolute temperature [22]. Depending on the material, it becomes important to keep detectors at low temperatures in order to avoid thermal excitations.

Electron-hole pairs created by incoming radiation may directly recombine in order to relax. The rate of this process may be enhanced by adding impurities with ± 1 electron. These impurities are called dopants and result in the addition of new intermediate energy levels. Furthermore, one can divide the doped materials into P-type and N-type semiconductors, having a deficit or surplus of electrons, respectively [22].

By combining the two types, one forms what is known as a depletion region or P-N junction, shown in Figure 8. Electrons and holes diffuse over the said junction, forming charged ions until reaching equilibrium. Additionally, one can increase the diffusion

across the junction (thereby widening the depletion region) by applying an external electric field with a reverse bias [19].

An important property of this region is its lack of mobile charge carriers, as the external electric field causes them to drift in opposite directions. By connecting the semiconductor detector to an appropriate set of electronics, one can detect electric signals generated by radiation in the form of drifting electron-hole pairs.

Semiconductors are popular partly due to their low ionization energy leading to a higher signal rates. A common choice is Si, due to its reasonable energy resolution and signal output without the need of liquid nitrogen cooling and cheap production.

3.4 The R^3B calorimeter - CALIFA

CALIFA will be able to detect light charged particles and γ-rays up to $\sim$300 MeV and 30 MeV, respectively [12]. Table 1 shows the energy resolution specifications. The design of CALIFA is based on the experience from the previous setup, ALADIN-LAND, which currently exists at GSI. In comparison, the Crystal ball spectrometer of ALADIN-LAND has a resolution of 7% for 1.3 MeV γ rays and $\sim$12% sum resolution [23]. In addition, the geometry of CALIFA will be better optimized for Doppler correction in inverse kinematics for R^3B experiments.

The CALIFA barrel section covers the polar angles 43° to 140.3°. Sixteen sectors (called petals) are needed for full azimuthal angular coverage, each comprising 16 carbon fiber pockets in a honeycomb structure. Each pocket contains in turn four scintillating crystals. A schematic of CALIFA and the detection range for the barrel can be seen in Figure 9. The sectors have a high granularity in order reduce the Doppler broadening experienced due
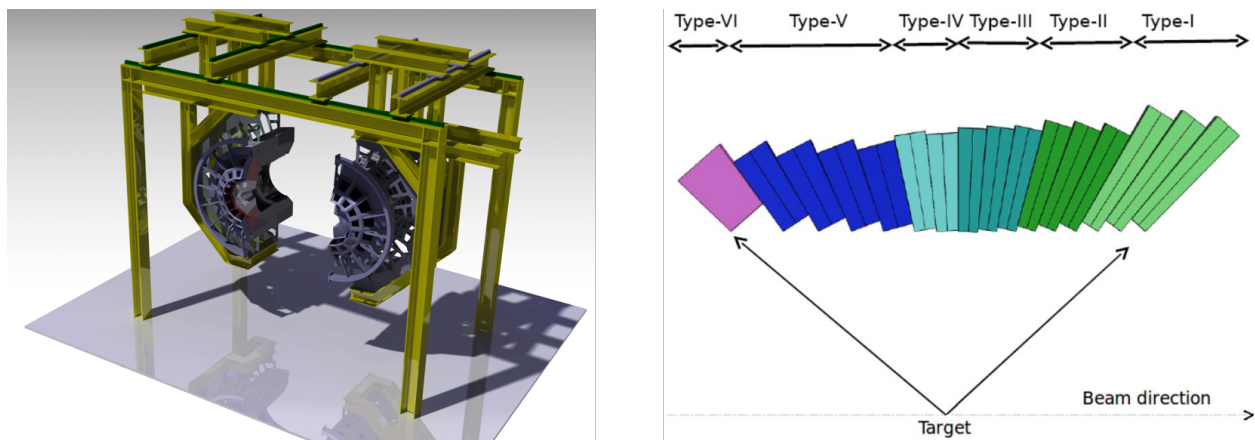

Figure 9: Left panel: 3D model of the CALIFA barrel. Right panel: CALIFA barrel detection range with respect to the target [12].

14

to the high energy beams. In the laboratory frame, the Lorentz transformation affects the γ ray energy E_γ^L as given by eq. 14,

$$E_\gamma^L = \frac{E_\gamma^{PF}}{\gamma} \cdot \frac{1}{1 - \beta cos\theta} \qquad (14)$$

with $\beta = \frac{v}{c}$, $\gamma = \frac{1}{\sqrt{1-\beta^2}}$ and E_γ^{PF} being the γ-ray energy in the rest frame of the particle beam. If one has detected the polar angle of the emitted γ ray, one can calculate the relative resolution using eq. 15,

$$\frac{\Delta(E_\gamma^{PF})}{E_\gamma^{PF}} = \frac{\beta sin\theta}{1 - \beta cos\theta} \cdot \Delta(\theta) \qquad (15)$$

with the polar angle uncertainty $\Delta(\theta) = k_1 \frac{1 - \beta cos\theta}{\beta sin\theta}$, where k_1 is a contribution to the energy resolution due to Doppler broadening [12].

Table 1: Performance goals for the CALIFA detector [12].

Energy resolution	1 MeV γ	$\frac{\Delta E}{E} < 7\%$
Sum energy resolution	3 MeV γ	$\frac{\Delta E}{E} \leq 10\%$
Light charged particles	≤ 320 MeV	$\frac{\Delta E}{E} = 1\%$
Proton-γ separation	1 to 30 MeV	

When designing a scintillation detector, the choice of material is important. Scintillators can be divided into different subgroups, each with pros and cons. For CALIFA, γ-ray energy resolution and high stopping power of protons were of high importance. Therefore, an inorganic crystal scintillator was chosen since these generally have high Z and density.

Table 2: Properties of scintillation materials considered for CALIFA Barrel [12].

Material	CsI(Tl)	LaBr$_3$(Ce)	LaCl$_3$(Ce)	NaI(Tl)
Density (g/cm^3)	4.51	5.29	3.86	3.67
Light Output (photons/MeV)	52k	63k	49k	39k
Sensitivity peak (nm)	550	380	350/430	310/415
Decay constant (ns)	700/3300	25	25/213	620/230
Hygroscopic	Slightly	Yes	Yes	Yes
Radiation Length (cm)	1.86	1.881	2.813	2.59

Table 2 gives specifics for a few materials. $LaBr_3(Ce)$ and $LaCl_3(Ce)$ are new materials with relatively short decay constants and high light output. CsI(Tl) has the advantage of being only slightly hygroscopic while having relatively high light output. In comparison, a classical material, such as NaI(Tl), has the disadvantage of being hygroscopic and having a relatively low light output. The selection of scintillating material for the barrel was made based on these considerations, particularly its hygroscopic properties, and moderate cost. In addition, the CsI(Tl) scintillation spectrum has a strong overlap with the effective detection range of the APD (Avalanche PhotoDiode) S8664-1010 from Hamamatsu used for light detection of the crystal [12]. CALIFA contains six general crystal geometries, with lengths 17, 18 or 22 cm grouped into sectors of 64 crystals. The general shape is that of a trunkated pyramid, as can be seen in Figure 10.
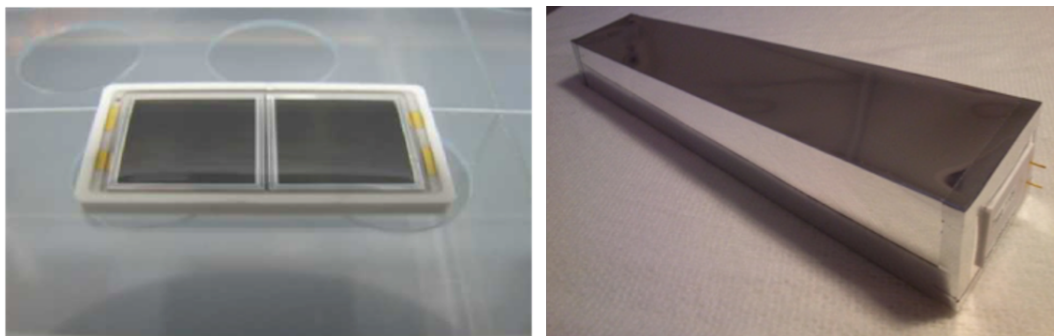

Figure 10: Left panel: photograph of the APD from Hamamatsu used for scintillation light readout. The right hand photograph shows a CALIFA crystal wrapped in reflective foil with APD mounted.

4 Experiment and data analysis

4.1 The experiment

The experiment took place in November 2017 at Centrum Cyklotronowe Bronowice (CCB), Kraków. Studies are conducted at CCB in many areas such as medical physics, radiobiology and nuclear physics. Proton beams with energies of 70-230 MeV and currents up to 500 nA can be delivered to the experimental setups [24].

In the future R^3B experiments, complete kinematic reconstruction of QFS events through particle tracking and energy measurements is of high importance. In order to partly attempt this, CALIFA was supplemented with a set of Si detectors for tracking.

The γ energy calibration of the CALIFA petals was performed with a ^{60}Co source, which emits γ rays at the energies of 1173 and 1332 keV. Proton beams at different energies were

also used for the CALIFA proton calibration. Additionally, a ^{90}Sr source was used to test two Double Sided Silicon Strip detectors (DSSSD) target trackers. The Lund University (LU) petals were oriented in order to detect outgoing particles with scattering angles between 25 and 58 degrees, where the opening angle of the (p,2p) QFS reactions is around 80 degrees shared between two protons [10]. The distances of the petals from the target were chosen to align the focal point of the crystals with the target position. Targets for QFS reactions such as (p,2p) are listed in Table 3 together with complementary data concerning the runs.

Table 3: Proton separation energies (S_p), target thickness, total data size for different materials and beam current, with given beam energy of 200 MeV [25].

Material	S_p (keV)	Target Thickness	Data Size (Gb)	Beam Current (pA)[1]
[208]Pb	8 003 (5)	9.7 mg/cm^2	192.3	86- 90
[124]Sn	12 093 (20)	49 mg/cm^2	231.6	105
[112]Sn	7 552 (3)	49 mg/cm^2	196.0	102 - 104
[12]C (Plastic)	15 956.68 (1)	600 μm	157.8	103
[16]O (H$_2$O)	12 127.41 [2]	460[3] μm	233.4	85 - 104

The geometry of the setup is shown in Figure 11. Three petals containing 64 crystals each were used. Two of them (LU0 and LU1), tilted ca 20° with respect to the beam axis, were dedicated to detect protons from the and one petal (DA) to detect coincident γ rays. The average distance between target and petals was ∼30 cm. In addition, two DSSSDs were used to track the charged particles. These detectors had the dimensions 60.1 x 60.1 mm^2, the active area of 58.5 x 58.5 mm^2 and were ∼300 μm thick. Each DSSSD has 32 strips in the x- and y-directions with the pitch width of 1.8 and 1.6 mm, respectively [26].

The DSSSDs were placed between the target and the LU CALIFA petals to function as charged particle tracking detectors. Their purpose was to identify the scattering reactions occurring at the target position and separate out background scattering events in air along the beam direction. The DSSSD trackers were chosen to cover as much as possible the solid angle of the LU petals.

---

[1]A given target had different beam currents for different runs.
[2]The uncertainty of the separtaion energy of water is less than 5 eV.
[3]The thickness of the water refers to the diameter of the liquid water jet.
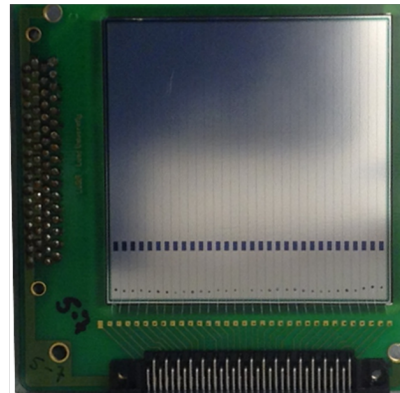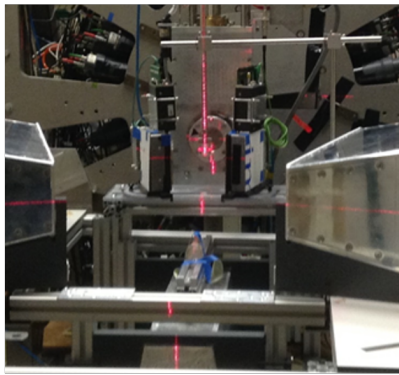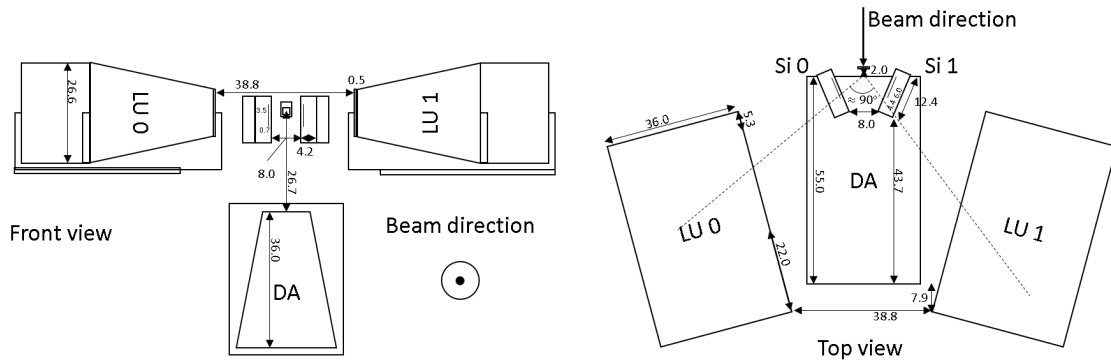
Figure 11: Top view of the experimental setup with distances in cm. The silicon detectors and LU petals (see text) were oriented in order to enable kinematic reconstruction of (p,2p) events. Furthermore, the DA Petal was situated directly under the target to detect γ rays emitted from the residual nuclei.

4.2 Data sorting and analysis

The purpose of the data sorting is to convert raw data into physical observables. When running the experiment, physical events were recorded by FEBEX3b modules and finally saved online in a binary list mode data format (.lmd) which is then unpacked, sorted and stored as .root files offline. FEBEX3b is a sampling analogue-to-digital converter (ADC) with 16 input channels, 60-MHz sampling rate and 14-bit resolution [27]. Once the signal has been digitized and stored locally in the module, it is read out by the event builder that processes the data and creates time-ordered events. The data is then accessed in order to write it out in a tree-like manner as shown in Figure 12. The GSI Object Oriented On-line Off-line system (Go4) which is based on ROOT was used for this purpose [28]. The data trees in the .root files contain Petal and DSSSD branches, which hold event information. The data is stored in a leaf-like structure under the corresponding branches. Each leaf contains information on one of the following quantities: energy, time, detector ID, fast and slow scintillation components. This data was then used to produce 2D plots such as

tracking, coincidence relations, reconstructive particle identification (RPID) and energy spectra, as discussed in following sections.

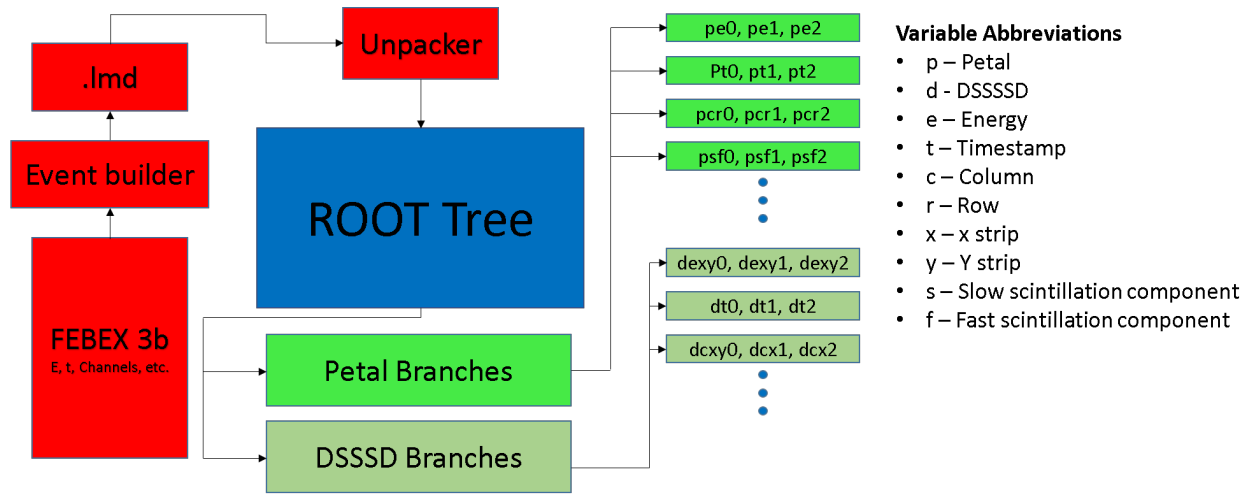**Figure 12:** Schematic of how events are stored and accessed. The red boxes contain raw data which are to be sorted into .root files. The data is sorted in a tree-like structure in which the branches correspond to either the Petal or DSSSD detectors, and the leaves correspond to the sorted data. Furthermore, the variable abbreviations belonging to each leaf are explained in bullet-points in the figure.

5 Results and Discussion
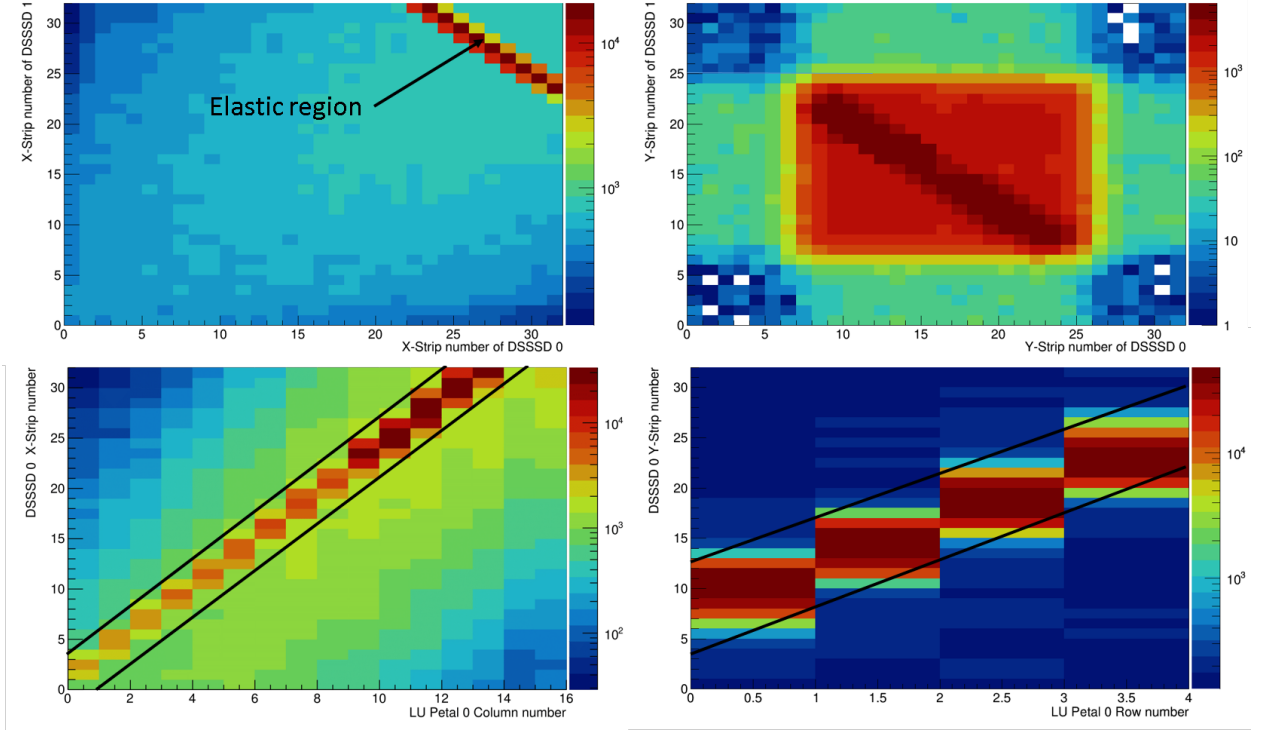
5.1 Tracking cuts

Figure 13: Top figures: DSSSD strip correlations. Bottom figures: CsI(Tl) and Si detector correlations. See text for details.

In a (p,2p) reaction, as indicated before, the opening angle of the outgoing particles are $\sim 90°$. Therefore there will be high-statistics correlations between the particle directions and detected energies in pairs of detectors after the (p,2p) reaction. This is illustrated in Figure 13, where the upper left panel shows x-side strips of the two DSSSDs hit by two coincident particles from the H_2O target. The anti-correlated high-statistics band is due to the elastic scattering events on hydrogen with this fixed opening angle of $\sim 90°$. The upper right panel shows the same as the left for the y-side strips. The diagonal band corresponds mostly to elastic scattering and off-diagonal entries are events where part of the azimuthal momentum is carried by the recoiling nucleus. Lower panels illustrate CsI(Tl) column/row to Si x/y-strip number correlation, which highlights the linear trajectory of the particles coming out of the reaction. By applying cuts in these kinematic relations one can reduce background arising from events not related to the reaction of interest. Different cuts were examined during this study in order to optimize the (p,2p) selection, particularly to extract γ rays from de-excitation of excited states.

5.2 RPID comparisons

RPID comprises different methods to distinguish different particles in the reaction. By applying cuts based on the RPIDs one can narrow down on the events belonging to (p,2p) reactions. However, in order to lower the amount of background events (e.g. from elastic scattering with air) we demand particle coincidence, i.e, particles have to be simultaneously detected in both DSSSD-petal pairs with an energy threshold and a given DSSSD strip correlation (Figure 13). This lends itself to an interesting possibility to compare two different methods to extract RPID information.

By making use of equation 6 we can identify different particles, as the energy they deposit depends on their charges and masses. This is a well known technique called a ΔE-E telescope. On the other hand, the RPID from the CsI(Tl), as mentioned in section 3.2, is also implemented in the FEBEX3b for CALIFA as an algorithm with parameters derived from experiments. To compare these methods we sorted the H_2O data and applied the two RPID selection cuts (see Figure 16).

As part of this investigation, the scintillation RPID resulted in 31372 proton events. Of these, 26534 also ended up in the ΔE-E cut. The 4838 events that ended up outside the proton cut of the ΔE-E plot were projected back to the scintillation RPID diagram. These events were found to be evenly distributed inside the scintillation RPID cut. The majority of events are probably due to the incomplete charge collection in the DSSSD as they fall below the proton selectiton cut. Similar results were found for the deuteron, as shown in lower right hand panel of Figure 16. Amongst the 28858 proton events identified using the ΔE-E cut, 2324 were misidentified mostly as γ rays by the RPID algorithm in the FEBEX3b. This shows that the accuracy of the current RPID scheme is within the range of 85-92%.

To investigate different types of reactions induced by the proton beam on different targets, reconstructive particle identification (RPID) plots were analysed. Figure 16 is one such plot, consisting of comparing the fast and slow scintillation components from the CsI(Tl) detectors. Hence, by applying appropriate cuts, (p,2p) and other types of events can be selectively analysed.
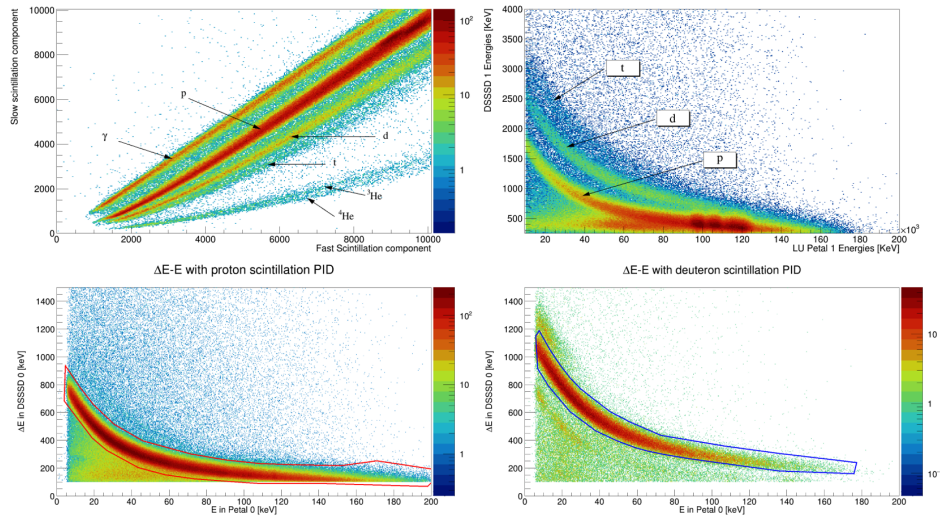
Figure 14: Upper Left panel: comparing the fast and slow scintillation components. As CsI(Tl) has discernibly different time constants for charged particles one can identify and cut out the non-essential events. Upper Right panel: result of the RPID in H_2O plotting the energy deposited in the petal versus the energy deposited in the DSSSD. Lower panels: protons and deuterons respectively selected by the CsI(Tl) RPID and projected onto the ΔE-E spectra.

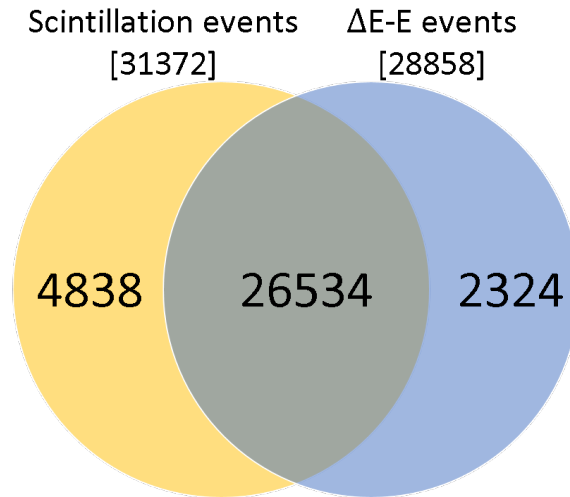

Figure 15: RPID statistics of protons in a subset of data with the H_2O target. The numbers above the Venn diagram represent the total numbers of protons determined by the respective methods. The middle number in the Venn diagram is the result of both RPID cuts applied, and the numbers on the sides represent the events which satisfy one condition and not the other. See text for details.
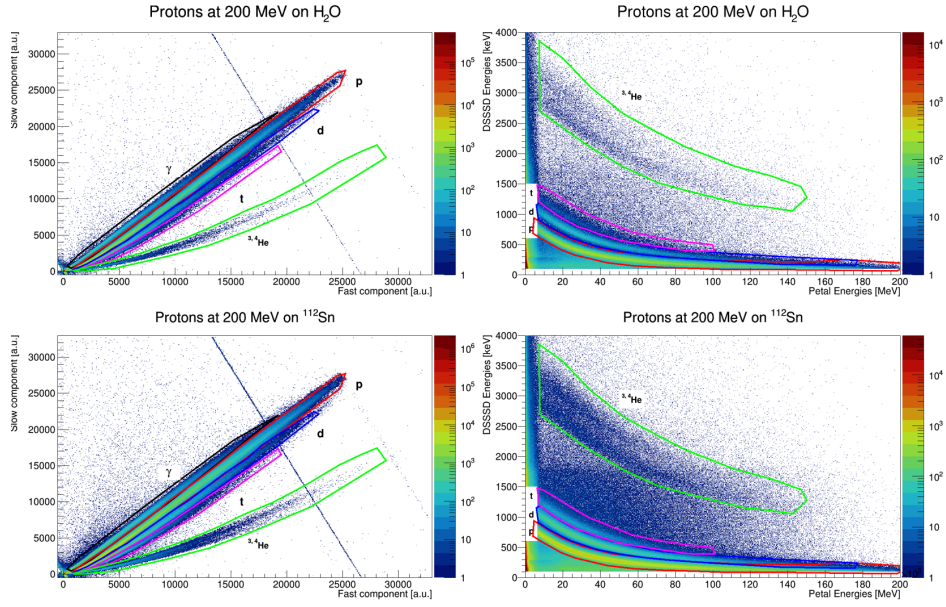
Figure 16: CsI(Tl) particle selection cuts on H_2O and ^{112}Sn targets used for the data in Tables 4 and 5.

Table 4: Accumulated number of particles using CsI(Tl) RPID. The ratios of particles normalized to the number of detected protons are described by $R_d(\%)$, $R_t(\%)$ and $R_{He}(\%)$. The statistical uncertainties in counts and ratios are below 2500 and 0.04%, respectively.

Target	Detector	Protons	Deuterons		Tritons		^{3,4}He	
			Counts	$R_d(\%)$	Counts	$R_t(\%)$	Counts	$R_{He}(\%)$
H_2O	0	1.3e+06	1.7e+05	13.2	2.0e+04	1.5	1.5e+04	1.1
	1	1.2e+06	1.2e+05	10.5	1.7e+04	1.5	4.3e+03	0.4
	2	5.6e+05	2.6e+04	4.6	3.3e+03	0.6	3.4e+03	0.6
^{112}Sn	0	5.4e+06	7.3e+05	13.7	9.2e+04	1.7	5.8e+04	1.1
	1	5.1e+06	5.7e+05	11.1	8.4e+04	1.6	1.9e+04	0.4
	2	2.5e+06	1.0e+05	4.1	1.4e+04	0.6	1.4e+04	0.6
^{124}Sn	0	3.1e+06	4.5e+05	14.6	6.6e+04	2.1	3.3e+04	1.1
	1	3.0e+06	3.5e+05	11.8	6.1e+04	2.0	1.1e+04	0.4
	2	1.5e+06	6.6e+04	4.5	9.4e+03	0.6	8.8e+03	0.6
Air	0	3.4e+05	4.7e+04	14.0	5.3e+03	1.6	4.2e+03	1.3
	1	3.1e+05	3.4e+04	11.2	4.6e+03	1.5	1.2e+03	0.4
	2	1.5e+05	7.7e+03	5.0	9.5e+02	0.6	9.4e+02	0.6

Table 5: Accumulated number of particles using $\Delta E\text{-}E$ RPID. R_N is the scaling factor used to compare the results for the different targets to the background measurement (air). The DSSSD-petal pairs are designated as left and right arms. The statistical uncertainties in counts and ratios are below 2500 and 0.05%, respectively. In order to calculate δR_N one used the uncertainties in beam current (1 pA) and detector live time (1 s).

Target	R_N	Arm	Protons	Deuterons		Tritons		^{3,4}He	
				Counts	R_d(%)	Counts	R_t(%)	Counts	R_{He}(%)
H_2O	2.90(5)	Left	1.2e+06	1.5e+05	12.7	2.6e+04	2.2	1.6e+04	1.3
		Right	1.1e+06	1.3e+05	12.1	2.3e+04	2.1	4.8e+03	0.4
^{112}Sn	8.90(13)	Left	5.0e+06	6.5e+05	13.1	1.2e+05	2.4	6.6e+04	1.3
		Right	4.7e+06	6.1e+05	13.0	1.1e+05	2.4	2.5e+04	0.5
^{124}Sn	5.24(8)	Left	2.9e+06	3.9e+05	13.8	7.6e+04	2.7	3.5e+04	1.2
		Right	2.8e+06	3.7e+05	13.4	6.9e+04	2.5	1.2e+04	0.4
Air	1.00	Left	3.1e+05	4.2e+04	13.5	7.4e+03	2.4	4.7e+03	1.5
		Right	2.8e+05	3.7e+04	12.9	6.4e+03	2.3	1.4e+03	0.5

The number of accumulated particles found by using the different RPID cuts given in Figure 15 are given in Tables 4 and 5. As can be seen, the relative production of deuterons, tritons and helium nuclei with respect to protons is largely consistent between the two methods with relative ratios falling from 12 to ~1%. The number of particles found with the Sn targets appears to be larger than that of the H_2O target, although one should note that the differences in target thicknesses are not considered in this comparison, further studies of these data sets can thus be made. An important point to know for the (p,2p) reaction analysis is that the particle production without target, i.e. the background, is significant. For this data no further relation between petals are used. The only requirement was a hit in a DSSSD and the corresponding CsI(Tl) detectors.

5.3 (p,2p) energy spectra and γ coincidences

The kinematic cuts and the RPID selections mentioned in the previous sections provide two of three important criteria to select the (p,2p) events. A third import signature is given by the energy of the two protons of the reaction.

Figure 17 shows the calibrated energies of the two tracked and identified protons detected in both LU0 and LU1 petals. The energy distributions are concentrated on the lines $y + x = C$, where C is the incoming proton energy for either elastic scattering events on hydrogen in H_2O or (p,2p) reactions on ^{16}O. To verify this (p,2p) reaction and investigate the possibility of knocking out a proton below the valence orbital, selection cuts on the summed proton energy spectra were applied. The top left panel in Figure 18 shows two regions of interest: the (p,2p) to ground state and $3/2^-$ excited state in ^{15}N.
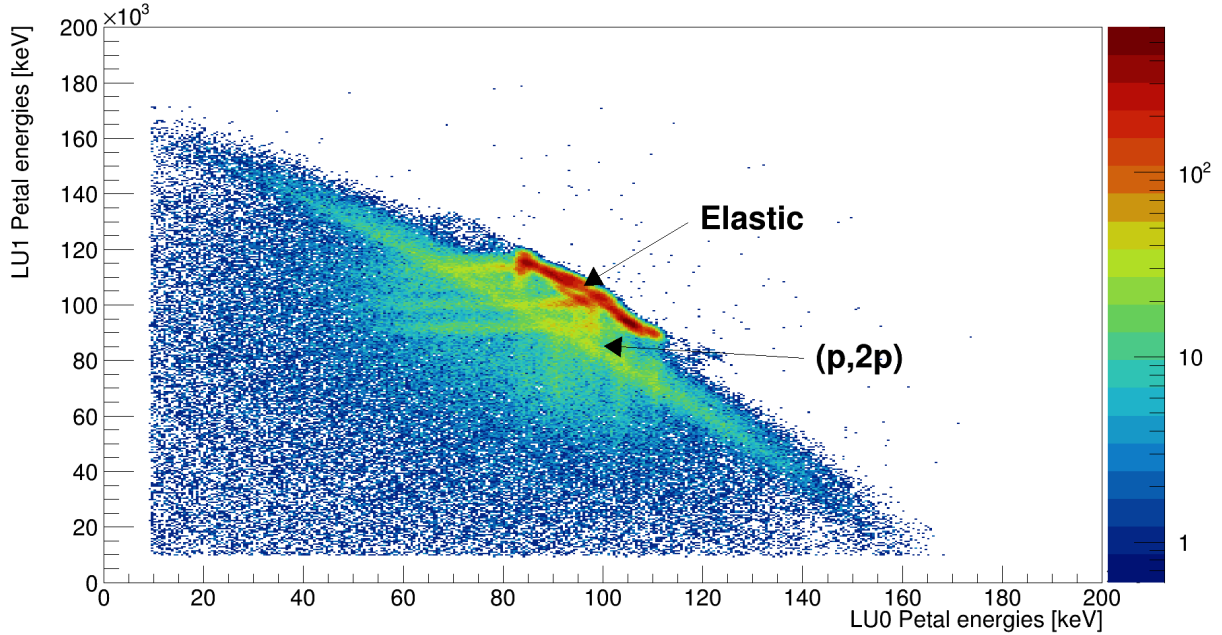
Figure 17: Energies detected in the LU0 and LU1 petals after applying two proton coincidence criteria. The most densely populated regions correspond to the elastic scattering events. A second band with a lower total energy indicates (p,2p) events.

By gating on the different regions, one can produce γ-ray energy spectra from the DA petal as shown in the top right panel in Figure 18. The region corresponding to the higher proton energy yielded no γ-ray peak, consistent with the population of the ground state. On the other hand, gating on the lower energy region yielded a γ-ray spectrum with a clear peak at 6.3 MeV. This γ-ray energy matches the excitation energy of the $3/2^-$ state of ^{15}N. This is a clear indication of (p,2p) reactions to multiple states in the ^{15}N nucleus.
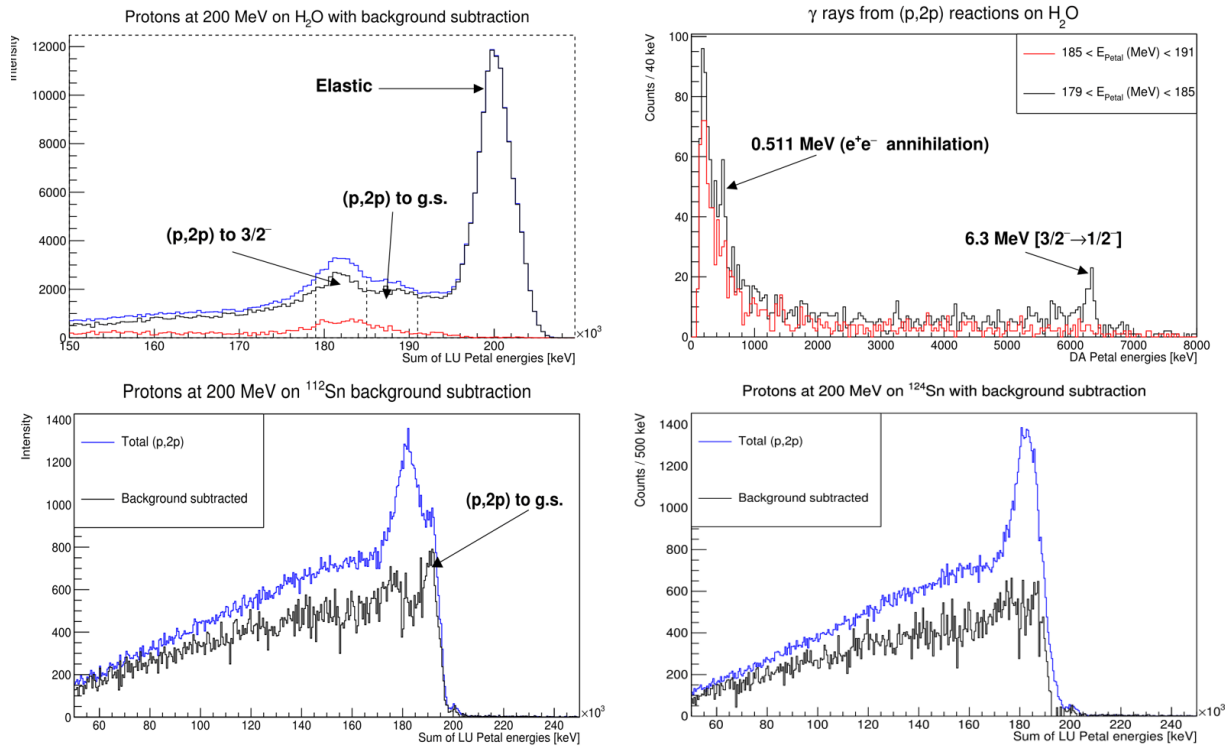
Figure 18: Energy spectra of different targets and reactions. Top left panel: sum energy spectra detected by the LU0 and LU1 petals. The points of interest are indicated by the arrows. A scaled background spectrum from running without target is shown in red, and the background subtracted spectrum is shown in black. The two regions marked by the vertical lines indicate coincidence regions used to produce γ-ray spectra in the top right panel. The de-excitation energy spectra show no discrete γ-ray lines in coincidence with (p,2p) to ground state while the 6.3 MeV γ ray is coincident with events inside the (p,2p) to $3/2^-$ window. Lower panels: Same as top left panel, but for the ^{112}Sn and ^{124}Sn targets. An indication of the (p,2p) to ground state reaction is indicated in the bottom left panel but is barely visible for the ^{124}Sn in the lower right panel.

Likewise, the summed proton energy spectra from the Sn targets were produced and analysed. In both cases the background subtraction with the data without any target removed peaks at $\sim$180 MeV. On the bottom right panel of Figure 18 the background subtracted spectrum from the ^{124}Sn target does not show a clear peak. However, the spectrum from the ^{112}Sn target suggests a small peak at $\sim$192 MeV, which is consistent with $S_p = 7.6$ MeV as listed in Table 3. Therefore, the identification of (p,2p) reactions to the ground state of ^{111}In may also have been accomplished.

6 Summary and outlook

Data from a (p,2p) QFS experiment with multiple targets at CCB, Kraków, was analysed. The experiment featured CsI(Tl) detector modules to be used in the upcoming R^3B experiments at GSI and FAIR, as well as a set of Si detectors.

The reaction events from the target were identified from background reactions using tracking cuts. Several different types of light particles from the scattering reactions were observed and identified using two different PID methods: fast/slow CsI(Tl) scintillation component comparison, and ΔE-E relationship between the Si and the CsI(Tl) detectors. As discussed in section 5.2, discrepancies in the range of 8-15% between the two PID methods were investigated and may be attributed to the limitations of the cuts, FEBEX3b algorithm or incomplete detection of the full energies of incoming particles in the detectors.

After examining the summed energy spectrum from the H_2O target and performing a rough proton energy calibration using the elastic scattering peak, (p,2p) reactions with ^{112}Sn and ^{124}Sn targets were compared. In ^{112}Sn, an indication of the (p,2p) reaction to the ground state $9/2^+$ in ^{111}In was observed.

By gating on the appropriate summed proton energy range of (p,2p) reactions from the H_2O target one could successfully produce a 6.3-MeV γ-ray peak corresponding to the known $3/2^- \rightarrow 1/2^-$ transition energy in ^{15}N.

The next step in the analysis of this experiment is to investigate the proton energy calibration data and to use the (p,p) elastic scattering cross section to extract efficiencies for proton detection in the petals. This could then potentially be used in order to extract the (p,2p) cross section in ^{16}O from this measurement. In the longer term, the use of the detectors for commissioning experiments at FAIR in the fall of 2018 is planned.

References

[1] Interactive chart of nuclides.
https://www.nndc.bnl.gov/nudat2/chartNuc.jsp.

[2] R^{3}B Experiments.
https://fair-center.eu/public/experiment-program/nustar-physics/r3b.html.

[3] I. Panov. Nucleosynthesis of heavy elements in the r-process. *Physics of Atomic Nuclei*, 79(2):159, 2016.

[4] FAIR.
https://www.gsi.de/en/researchaccelerators/fair.htm.

[5] GSI Experiments.
https://www.gsi.de/en/researchaccelerators/research_an_overview.htm.

[6] D. Cortina-Gil et al. CALIFA, a dedicated calorimeter for the r^{3}b/fair. *Nuclear Data Sheets*, 120:99 – 101, 2014.

[7] APPA.
https://www.gsi.de/en/work/research/appamml/atomic_physics/ap_und_-fair/sparc.htm.

[8] CBM.
https://fair-center.eu/for-users/experiments/cbm-and-hades/cbm.html.

[9] Antiproton research.
https://www.gsi.de/en/researchaccelerators/fair/research_with_fair/antipro-ton_physics.htm.

[10] V. Panin et al. Exclusive measurements of quasi-free proton scattering reactions in inverse and complete kinematics. *Physics Letters B*, 753:204, 2016.

[11] O. Tengblad. NUSTAR and the status of the r^{3}b project at fair. *Pramana - Journal of Physics*, 75(2):355, 2010.

[12] Technical report for the design, construction and commissioning of the CALIFA barrel: The R^{3}B CALorimeter for In Flight detection of γ-rays and high energy charged pArticles.
http://igfae.usc.es/~r3b/documentos/TDR/CALIFA_BARREL_TDR.pdf.

[13] M. Borri et al. Detector production for the r3b si-tracker. *Nuclear Instruments and Methods in Physics Research, Section A (Accelerators, Spectrometers, Detectors and Associated Equipment)*, 836:105, 2016.

[14] R^{3}B-GLAD superconducting magnet.
https://www.asgsuperconductors.com/doc/GLAD.pdf.

[15] Technical report for the design, construction and commissioning of NeuLAND: The high-resolution neutron time-of-flight spectrometer for R³B. https://edms.cern.ch/ui/file/1865739/1/TDR_R3B_NeuLAND_public.pdf.

[16] Kenneth S. Krane and David Halliday. *Introductory nuclear physics.* New York : Wiley, cop. 1988, 1988.

[17] M. Goeppert Mayer. The shell model. *Science*, (3636):999, 1964.

[18] Gerhard Jacob and Th. A. J. Maris. Quasi-free scattering and nuclear structure. *Rev. Mod. Phys.*, 38:121, Jan 1966.

[19] William R. Leo. *Techniques for nuclear and particle physics experiments : a how-to approach.* Berlin ; New York : Springer, 1994.

[20] Aafke Christine Kraan. Range verification methods in particle therapy: Underlying physics and monte carlo modeling. *Frontiers in oncology*, 5:150, 2015.

[21] Introduction to high energy astrophysics. http://astronomy.nmsu.edu/tharriso/ast536/ast536week8.html.

[22] Syed Naeem Ahmed. *Physics and engineering of radiation detection.* San Diego ; London: Academic Press, 2007.

[23] Crystalball. https://web-docs.gsi.de/~gsgweb/proj/cb_project.html.

[24] CCB Kraków. https://ccb.ifj.edu.pl/en.ncrh_ccb.html.

[25] W. Meng et al. The AME2016 atomic mass evaluation (II). Tables, graphs and references. *Chinese Physics C*, 41(3):030003, 2017.

[26] P. Golubev et al. The Lund–York–Cologne Calorimeter (LYCCA): Concept, design and prototype developments for a FAIR-NUSTAR detector system to discriminate relativistic heavy-ion reaction products. *Nuclear Instruments and Methods in Physics Research Section A: Accelerators, Spectrometers, Detectors and Associated Equipment*, 723:55, 2013.

[27] FEBEX3b specifications. https://www.gsi.de/fileadmin/EE/Module/FEBEX/febex3b.pdf.

[28] GSI Object Oriented On-line Off-line system (Go4). https://www.gsi.de/en/work/research/experiment_electronics/data_processing/data_analysis/the_go4_home_page.htm.